Progress in Additive Manufacturing (2018) 3:39–49
https://doi.org/10.1007/s40964-018-0048-0

FULL RESEARCH ARTICLE

Effects of powder characteristics and processing conditions on the corrosion performance of 17-4 PH stainless steel fabricated by laser-powder bed fusion

Harish Irrinki[1] · Talia Harper[2] · Sunil Badwe[3] · Jason Stitzel[4] · Ozkan Gulsoy[5] · Gautam Gupta[6] · Sundar V. Atre[1]

Received: 20 October 2017 / Accepted: 6 May 2018 / Published online: 24 May 2018

Abstract
Powder characteristics and processing conditions are known to strongly influence the densification of parts fabricated by the laser-powder bed fusion (L-PBF) process. However, the influence of powder and L-PBF process parameters on corrosion performance of parts has not been studied extensively. In this paper, the effects of processing conditions (energy density) and powder characteristics (shape and size) on the corrosion performance of 17-4 PH stainless steel parts produced by L-PBF were investigated. The corrosion performance of the L-PBF parts was evaluated using corrosion current, polarization resistance and corrosion rate values from the potentiostatic polarization curves. It was observed that the density and consequently corrosion performance of L-PBF parts using coarser water-atomized (D_{50} = 24 and 43 µm) powders increased when the energy density was increased from 64 to 104 J/mm^3. However, the density and subsequent corrosion performance of the L-PBF parts was relatively higher for the finer gas (D_{50} = 13 µm) and water-atomized (D_{50} = 17 µm) powders when fabricated using the same range of energy densities. At an energy density of 104 J/mm^3, the corrosion performance of L-PBF parts fabricated using water-atomized 17-4 PH stainless steel powders all powders exhibited higher polarization resistance (28,000 ± 500 Ω) than the wrought sample (25,000 ± 1000 Ω) in the 0.5 M NaCl environment, indicative of better corrosion properties.

Keywords Laser-powder bed fusion · Corrosion · Stainless steel · Particle characteristics · Water-atomized powder · Gas-atomized powder

1 Introduction

Stainless steel alloys have been used in many applications due to their excellent strength and corrosion properties [1–4]. The laser-powder bed fusion (L-PBF) process has gained attention and importance due to its potential to produce complex-shaped parts for medical, tooling, automotive and aerospace industries [1, 5–8]. The L-PBF process is layer by laser melting or fusion process which uses a laser beam to melt the starting powder for fabricating a desired 3D component [1–4]. Among stainless steels, 17-4 PH stainless steel is desirable for fabrication of parts using L-PBF process in transportation (engine components, gears, fuel injectors) and injection molding industries (injection mold

✉ Sundar V. Atre
sundar.atre@louisville.edu

Harish Irrinki
harish.irrinki@louisville.edu

Talia Harper
ttaharper41@gmail.com

Sunil Badwe
sunilbadwe@gmail.com

Jason Stitzel
jason.stitzel@mtialbany.com

Ozkan Gulsoy
ogulsoy@marmara.edu.tr

Gautam Gupta
gautam.gupta@louisville.edu

1 Materials Innovation Guild, University of Louisville, Louisville, KY 40292, USA

2 Alabama State University, Montgomery, AL 36104, USA

3 North American Höganäs, Johnstown, PA 15935, USA

4 Metal Technologies Incorporated, Albany, OR 97322, USA

5 Marmara University, Istanbul 34722, Turkey

6 Chemical Engineering Department, University of Louisville, Louisville, KY 40292, USA

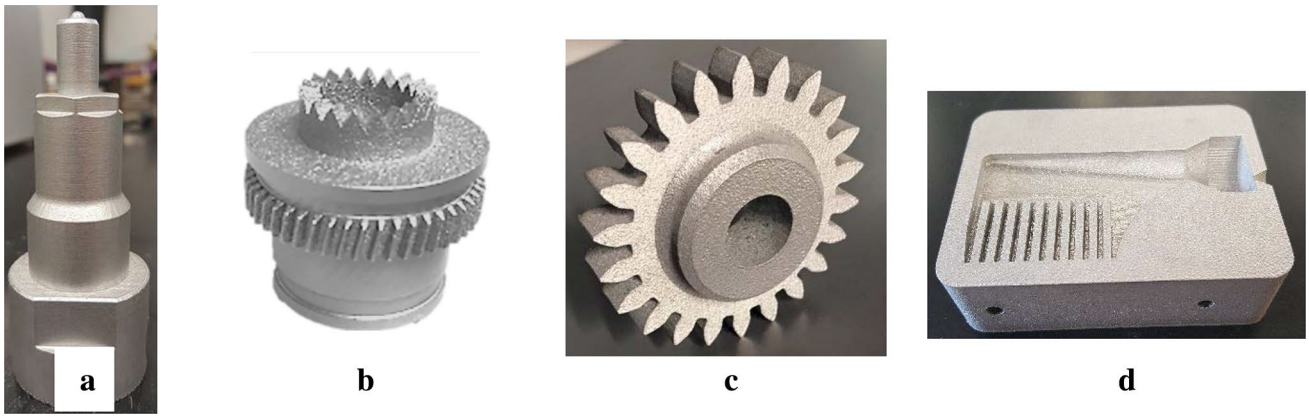

Fig. 1 17-4 PH stainless steel L-PBF parts fabricated by our research group in design collaboration with various industries: **a** fuel injector with conformal cooling channels (Cummins, Columbus, OH); **b** helicopter engine part (Helicopter Transport Services, Portland, OR); **c** automotive engine gear (Cummins, Columbus, OH); **d** plastic injection mold with conformal cooling channels (Amaray Plastic Inc., Elizabethtown, KY)

with conformal cooling channels) within our research group as shown in Fig. 1.

Many research studies have been carried out to understand the effects of powder and processing conditions on the densification behavior and structural attributes of components fabricated by the L-PBF process [1, 3, 7, 9–15]. Most of the prior studies indicated that quality of parts produced using the L-PBF process depends on many factors, the most important being processing conditions and powder characteristics. The effect of processing conditions such as laser power, scan speed, layer thickness, scan spacing on the densification of powders has been extensively studied in recent years [1–4]. On the other hand, in-depth experimental studies on the influence of powder characteristics such as powder shape, size on the densification behavior have been reported only in the recent past [2, 5]. The variation in densification phenomena of the powder as a function of powder type and processing conditions could lead to porosities in the parts fabricated using L-PBF process [1, 3, 7, 9–15].

The porosity in L-PBF parts fabricated using stainless steel powders could not only affect the mechanical properties but also influence the sensitivity to localized corrosion attack, especially in the corrosion environments [16–19]. However, the corrosion properties of L-PBF components fabricated from powders with different characteristics and in different processing conditions have not received much attention in the literature. The corrosion resistance of stainless steel parts results from a thin and protective passive film chromium oxide (Cr_2O_3) or iron oxide (Fe_2O_3)-based passive film. The chromium or iron oxide passive film acts as a partial barrier between the metal and the corrosive species present in the environment [16, 18, 20–23]. The stability of the passive film when exposed to aggressive corrosive species such as chloride ions is important in preventing corrosion [16, 18, 20, 22–25]. However, the porosity in L-PBF parts can be expected to compromise the passive film layer stability and could result in enhanced corrosion of the L-PBF parts [16–19, 26]. Therefore, it is important to understand the corrosion behavior of 17-4 PH stainless steel components built using L-PBF process in natural service conditions.

Independent corrosion studies in various electrolytes have been reported on 17-4 PH stainless steel L-PBF parts fabricated using gas-atomized powders [16, 18, 20, 21, 23, 25]. However, few studies have been reported that compare the corrosion resistance of the 17-4 PH stainless steel L-PBF parts fabricated from powders of different characteristics such as shape, size and the method utilized for atomization (gas-atomized or water-atomized) [16, 18]. In order to address this gap in the literature, the present study was carried out to understand the effect of powder characteristics and processing conditions on the corrosion performance of 17-4 PH stainless steel L-PBF parts. The results from the current study will provide a better understanding of the effect of porosity, density and microstructures on the corrosion performance of 17-4 PH stainless steel L-PBF gas- and water-atomized parts.

2 Experimental materials and methods

One 17-4 PH stainless steel gas-atomized powder and three water-atomized powders were used in this study. The gas-atomized 17-4 PH stainless steel powder utilized for this study was supplied by 3D Systems. The water-atomized 17-4 PH stainless steel powders were obtained from North American Höganäs. A high-resolution FEI Quanta 600F scanning electron microscope (SEM) was used for morphology

analysis of the powders. The L-PBF experiments were performed on a 3D Systems ProX 200 machine in an argon environment. The tensile geometries were fabricated using four energy densities to melt the powders, i.e., 64, 80, 84 and 104 J/mm^3. The energy densities were calculated using the laser processing parameters like laser power, scan speed, hatch spacing and layer thickness. In this study, two laser powers (150 and 195 W) and two scan speeds (1250 and 1550 mm/s) were used to fabricate the tensile geometries while layer thickness and hatch spacing were kept constant at 30 and 50 µm, respectively.

A total of 64 parts from four powders in four processing conditions were fabricated during the study. Of the 64 parts, four parts fabricated from each powder type and in one processing condition were selected for Archimedes density and corrosion performance analysis. Density measurements were conducted using the Archimedes method on a Mettler Toledo XS104 weighing balance. The density values of the 17-4 PH stainless steel gas- and water-atomized L-PBF parts were expressed as a percentage relative to the density of the 17-4 PH stainless steel cast part (7.87 g/cm^3). The porosity of L-PBF parts was calculated using Eq. 1:

$$\phi = 1 - \frac{\rho\,(l)}{\rho\,(t)}, \tag{1}$$

Fig. 2 Electrochemical corrosion studies setup used in this study

where ϕ is the porosity of the L-PBF parts, $\rho(l)$ is the density of the L-PBF parts, $\rho(t)$ is the density of 17-4 PH stainless cast part.

Potentiostatic polarization experiments were used to compare the electrochemical or corrosion behavior of the test coupons. All polarization experiments were conducted in an electrochemical glass cell shown in Fig. 2. Metrohm Autolab PGSTAT100N was used to perform three-electrode electrochemical measurement. Ag/AgCl was used as a reference electrode and the platinum was used as a counter electrode. The polarization experiments were carried out on L-PBF parts by varying the potential from 1 to −1 V/Ag/AgCl. The surface area of 1 cm^2 of each L-PBF part, which was finished with 1200 grit SiC paper, was exposed to the 0.5 M NaCl solution in ambient conditions. All experiments were carried out at room temperatures and were repeated 3 times for each specimen.

A summary of 17-4 PH stainless steel particle characteristics used in this study is reported in Table 1 [27, 28]. The morphology (shape and size) of the powders was characterized using SEM and shown in Fig. 4, showing the gas-atomized powders to be spherical while the water-atomized powders were irregular in shape (Fig. 3).

3 Results

The variation of density as a function of the energy density used to fabricate L-PBF parts using four 17-4 PH stainless steel powders are reported in Table 2.

The densities of L-PBF parts produced using coarser water-atomized powders (D_{50} = 24 µm and 43 µm) were lower when compared to the density of L-PBF parts produced using the finer gas-atomized (D_{50} = 13 µm) and water-atomized (D_{50} = 17 µm) powders (97 ± 0.5%) at low energy densities of 64 and 80 J/mm^3. The high density of the L-PBF parts (97 ± 0.5%) fabricated using finer gas-atomized (D_{50} = 13 µm) and water-atomized (D_{50} = 17 µm) powders can be attributed to their high tap (4 ± 0.05 g/cc) and apparent density (3 ± 0.05 g/cc) (Table 2). Lee et al. [29] showed that high apparent density of powders could result in better packing density of the powder bed. The high packing density of the powder bed presumably results in better melt pool

Table 1 Particle characteristics of the 17-4 PH stainless steel gas- and water-atomized powders

Powder	Particle distribution			Tap density (g/cc)	Apparent density (g/cc)
	D_{10} (µm)	D_{50} (µm)	D_{90} (µm)		
Gas-atomized (*G*)	5	13	27	4 ± 0.05	3 ± 0.002
Water-atomized (*W*)1	10	17	28	4.3 ± 0.05	3 ± 0.05
Water-atomized (*W*)2	16	24	37	3.7 ± 0.01	2.8 ± 0.05
Water-atomized (*W*)3	26	43	67	3.7 ± 0.05	2.8 ± 0.05

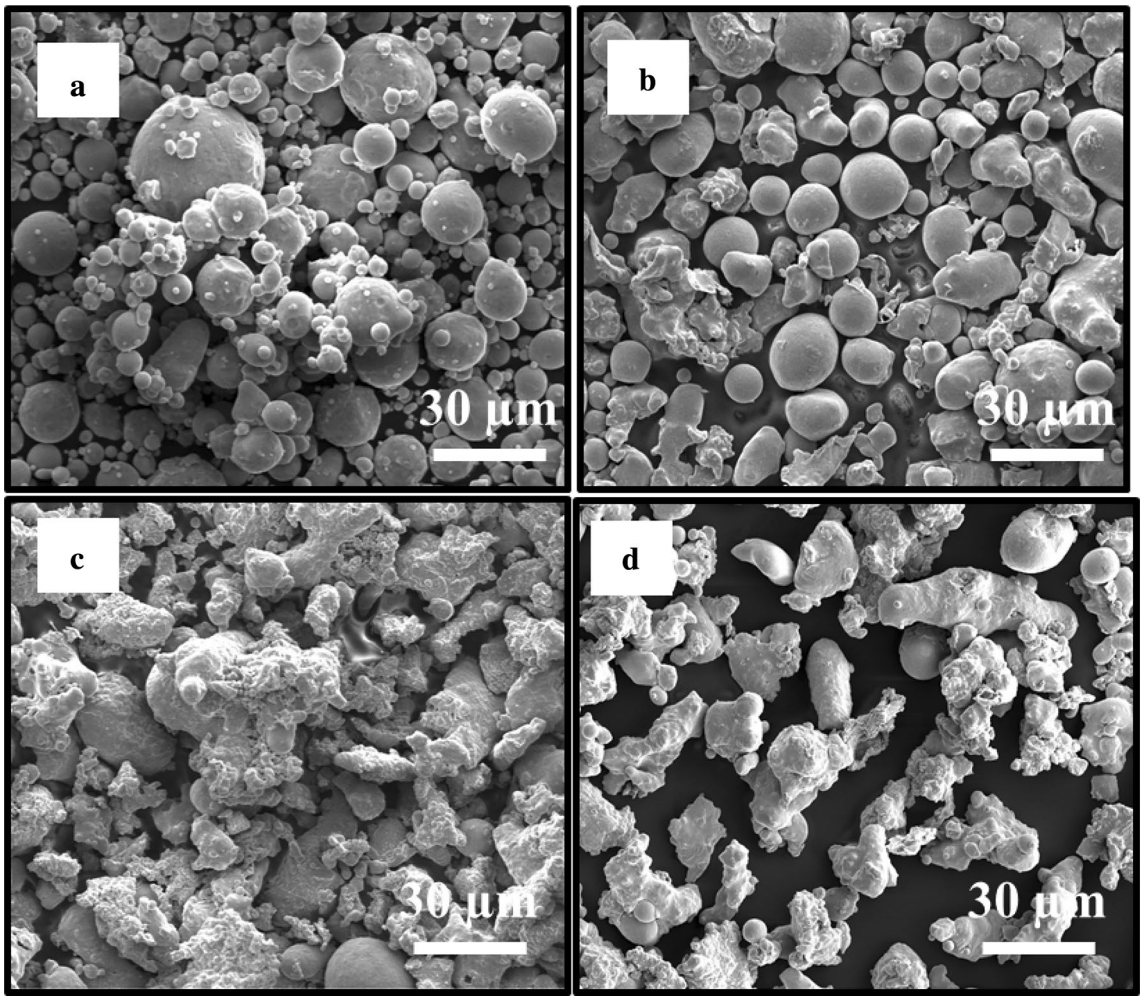

Fig. 3 SEM images of the 17-4 PH stainless steel gas- and water-atomized powders used in this study: **a** gas-atomized powder (D_{50} = 13 µm); **b** water-atomized powder (D_{50} = 17 µm); **c** water-atomized powder (D_{50} = 24 µm) and **d** water-atomized powder (D_{50} = 43 µm)

hydrodynamic stabilities ensuing enhance densification of the powders during the L-PBF process [27, 29–32]. However, the density of three 17-4 PH stainless steel water-atomized powders is similar (97 ± 0.5%) and comparable to 17-4 PH stainless steel gas-atomized powders when processed at high energy densities 84 and 104 J/mm^3. At higher energy densities, a large amount of molten pool with low viscosity and better wettability properties is likely to be formed in the powder bed producing high dense L-PBF part s [27, 29–32].

The variation in Tafel plots curves as a function of the energy density used to fabricate L-PBF parts from the four 17-4 PH stainless steel powders is shown in Fig. 4. The Tafel plots curves shown in Fig. 4 qualitatively indicated different anode and cathode curve behavior in 17-4 PH stainless steel gas- and water-atomized L-PBF parts when fabricated at different energy densities. The quantification of the Tafel plots behavior was subsequently performed to further understand the effect of density on the corrosion performance of four 17-4 PH stainless steel powders. Using the Tafel plot quantification method [16, 18], the 17-4 PH stainless steel L-PBF parts Tafel plots were analyzed as shown in Fig. 5 for calculating the corrosion current, i_{corr} and Tafel constants. The corrosion current, i_{corr} and Tafel constants were used to determine the polarization resistance R_p and corrosion rate from Eqs. 2 and 3, respectively:

$$\text{Polarization resistance}, R_p = \frac{1}{i_{corr}}\left(\frac{\beta_a \beta_c}{\beta_a + \beta_C}\right), \tag{2}$$

where the Tafel constants (β_a and β_c) represent the anodic and cathodic slopes, respectively.

$$\text{Corrosion rate, CR} = \frac{i_{corr}}{dA}(k \times \text{EW}), \tag{3}$$

where d is the density of the material (kg/m^3), A is exposed surface area of the material to corrosion (m^2), k is a constant

Table 2 Densities (expressed as % theoretical) of the 17–4 PH stainless steel gas- and water-atomized L-PBF parts fabricated under energy densities ranging from 64 to 104 J/mm^3

L-PBF parts from	Energy density 64 J/mm^3 (%)	Energy density 80 J/mm^3 (%)	Energy density 84 J/mm^3 (%)	Energy density 104 J/mm^3 (%)
Gas-atomized $D_{50}=13$ µm	97 ± 0.5	97.5 ± 0.5	97.5 ± 0.5	97.5 ± 0.5
Water-atomized $D_{50}=17$ µm	96 ± 1	97 ± 0.5	97 ± 0.5	97 ± 0.5
Water-atomized $D_{50}=24$ µm	87 ± 0.5	91 ± 0.5	96 ± 1	97 ± 0.5
Water-atomized $D_{50}=43$ µm	89 ± 0.5	95 ± 0.5	97 ± 0.5	97 ± 0.5

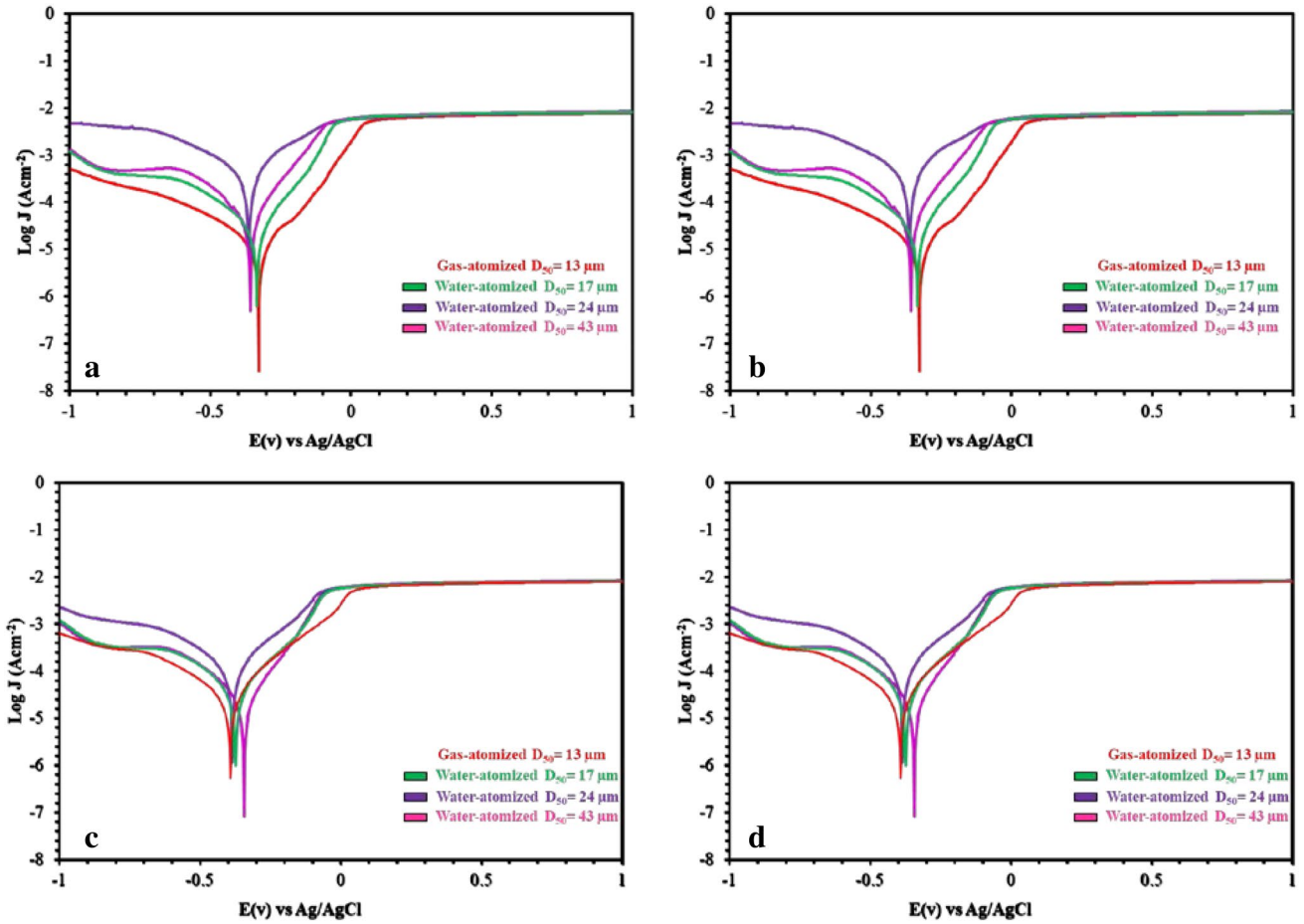

Fig. 4 Tafel plots of the components fabricated from four 17-4 PH stainless steel powders fabricated at **a** energy density 64 J/mm^3, **b** energy density 80 J/mm^3, **c** energy density 84 J/mm^3 and **d** energy density 104 J/mm^3

(3.272 m/year), and EW is the equivalent weight of the material.

The variation in corrosion current with the density of the L-PBF parts fabricated using finer gas-atomized ($D_{50}=13$ µm) and water-atomized ($D_{50}=17$ µm) powders is shown in Fig. 6a. High density and low corrosion current were observed for the 17-4 PH stainless steel L-PBF parts irrespective of the atomization technique to produce starting powders and the energy density of these two systems. The corrosion current of the gas-atomized ($D_{50}=13$ µm) and water-atomized ($D_{50}=17$ µm) L-PBF parts ranged between 0.1 and 1.0 µA, which is lower than the wrought sample (0.9 ± 0.1 µA). It can also be seen from Fig. 6a that the corrosion current of the L-PBF parts was not significantly varied for finer gas ($D_{50}=13$ µm) and water-atomized ($D_{50}=17$ µm) powders when fabricated at different energy densities. Previous studies by Frankel et al. [33] showed that the low corrosion current could be an indication that the rate of electrochemical reaction is slow either because of the thick oxide film or low porosity on the surface of the L-PBF parts. Further, no systematic variation in the corrosion current was observed for high dense (97 ± 0.5%) gas-atomized

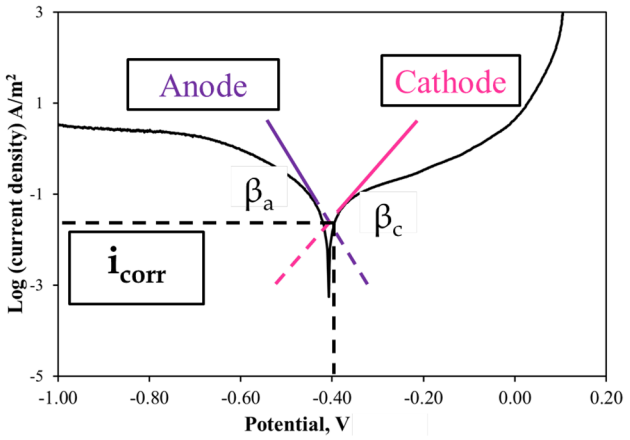

Fig. 5 Schematic diagram showing the extracting of corrosion current and constants from a Tafel plot

(D_{50} = 13 µm) and water-atomized (D_{50} = 17 µm) L-PBF parts when fabricated at different energy densities.

Figure 6b shows that the density and consequently corrosion current significantly varied as a function of energy density for coarser water-atomized powders (D_{50} = 24 µm and 43 µm) powders when compared to gas (D_{50} = 13 µm) and water-atomized (D_{50} = 17 µm) powders (Fig. 6a). The corrosion current decreased with increased density of the water-atomized (D_{50} = 24 and 43 µm) L-PBF parts. At a high energy density of 104 J/mm^3 and with densities higher than 97%, the corrosion current of the water-atomized (D_{50} = 24 and 43 µm) L-PBF parts was found to be lower than the wrought samples and similar to the corrosion current of gas (D_{50} = 13 µm) and water-atomized (D_{50} = 17 µm) L-PBF parts (Fig. 6). The corrosion currents of the 17-4 PH stainless gas- and water-atomized L-PBF parts with densities higher than 97% varied between 0.1 and 0.8 µA (Fig. 6b), whereas the corrosion current value wrought sample is 0.9 ± 0.1 µA. Similar corrosion current values for high dense 17-4 PH stainless steel parts fabricated with gas-atomized powders have been reported in previous L-PBF research studies [16–19, 26]. For example, Stoudt et al. [16] carried out potentiostatic polarization studies on L-PBF

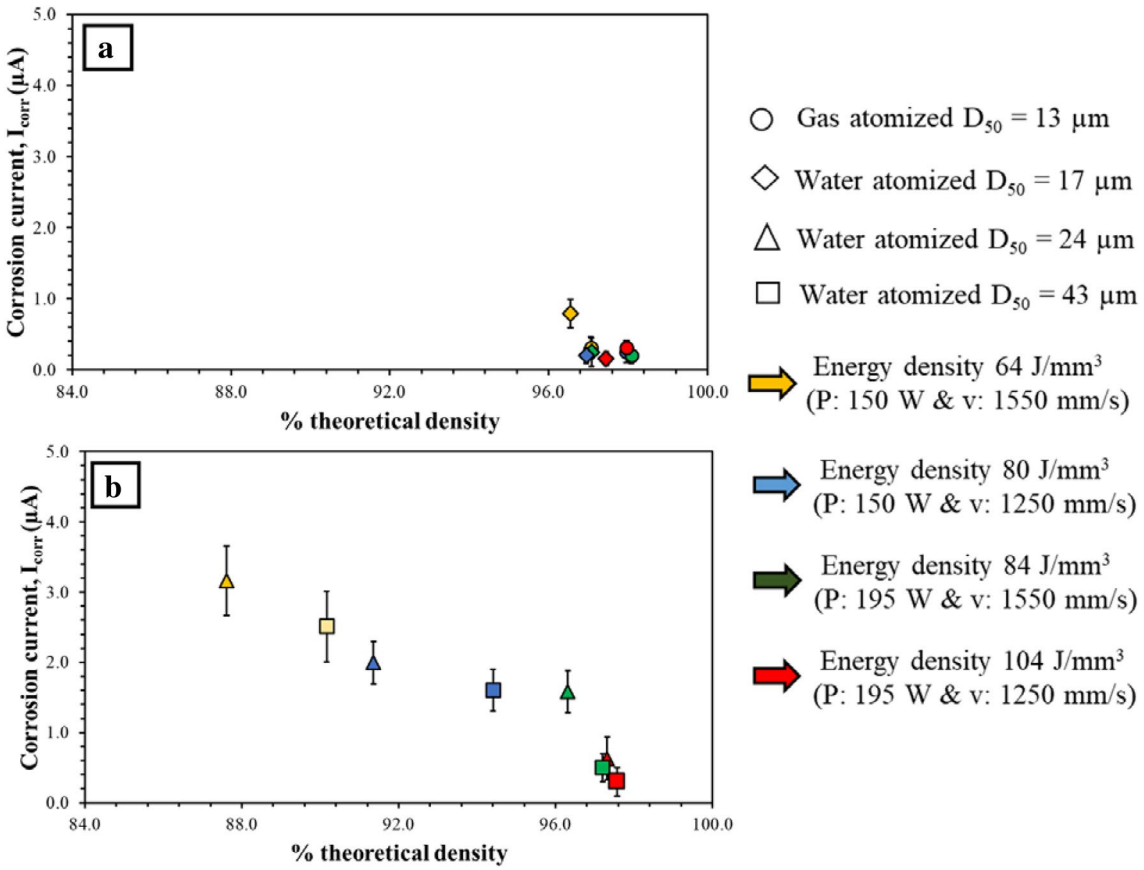

Fig. 6 Variation in corrosion current with % theoretical density and energy density for samples fabricated using: **a** gas-atomized (D_{50} = 13 µm) and water-atomized (D_{50} = 17 µm) powders, **b** water-atomized (D_{50} = 24 and 43 µm) powders. The symbols represent the four powders and the colors represent the four energy densities used in the fabrication

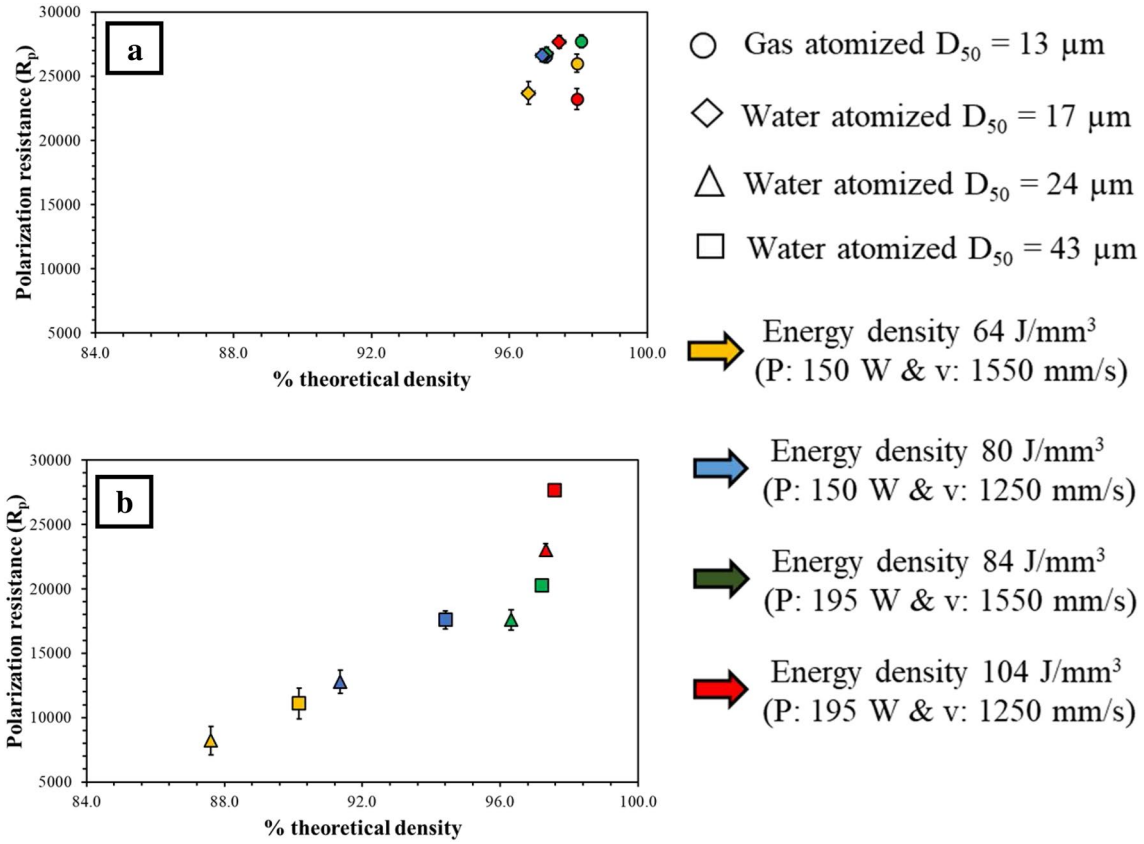

Fig. 7 Variation in polarization resistance as a function of % theoretical density and energy density for samples fabricated using: **a** gas-atomized (D_{50} = 13 µm) and water-atomized (D_{50} = 17 µm) powders, **b** water-atomized (D_{50} = 24 and 43 µm) powders. The symbols represent the four powders and the colors represent the four energy densities used in the fabrication

parts fabricated using 17-4 PH stainless steel gas-atomized powders in 0.5 M NaCl solution and reported that corrosion potential of the nearly fully dense (99 ± 0.5%) varied between 0.5 and 0.8 µA. Furthermore, at a high energy density of 104 J/mm^3, the corrosion current is independent of starting powder characteristics (shape and size) and atomization method (gas or water-atomization) used to produce these powders (Fig. 6).

In Fig. 7, the polarization resistance is plotted as a function of the density of L-PBF parts when fabricated using four 17-4 PH stainless powders at various energy densities. It was seen that the polarization resistance of the high dense (99 ± 0.5%) L-PBF parts fabricated using finer gas-atomized (D_{50} = 13 µm) and water-atomized (D_{50} = 17 µm) powders showed high polarization resistance (26,000 ± 2000 Ω) when fabricated at different energy densities (Fig. 7a). For comparison, these values are higher than wrought sample (25,000 ± 1000 Ω) and similar to the polarization resistance values (25,000–28,000 Ω) of 17-4 PH stainless steel L-PBF parts fabricated using gas-atomized powders as reported in the literature [14]. The high polarization resistance value of the L-PBF parts indicates that the resistance of the samples in the corrosion environment is high [21, 34, 35].

The density and consequently, the polarization resistance of coarser water-atomized powders (D_{50} = 24 and 43 µm) powders were found to be strongly dependent on energy density used to fabricate the samples (Fig. 7b). The polarization resistance of coarser water-atomized powders (D_{50} = 24 and 43 µm) L-PBF parts increased with an increase in energy density and density of the L-PBF parts. At low energy densities of 64 to 84 J/mm^3, the polarization resistance samples fabricated using coarser water-atomized powders (D_{50} = 24 and 43 µm) powders is 11,000 ± 3000 and 15,000 ± 4000 Ω, respectively. These polarization resistance values are lower than that of the finer gas- (D_{50} = 13 µm) and water-atomized (D_{50} = 17 µm) L-PBF parts as shown in Fig. 7.

Figure 7b also indicates that at high energy density of 104 J/mm^3, samples fabricated using coarser water-atomized powders (D_{50} = 43 µm) exhibited a slightly higher polarization resistance (28,000 ± 500 Ω) than samples fabricated using gas-atomized (D_{50} = 13 µm) powders (23,000 ± 1000 Ω) and wrought samples (25,000 ± 1000 Ω). Thus, the corrosion performance of the 17-4 PH stainless

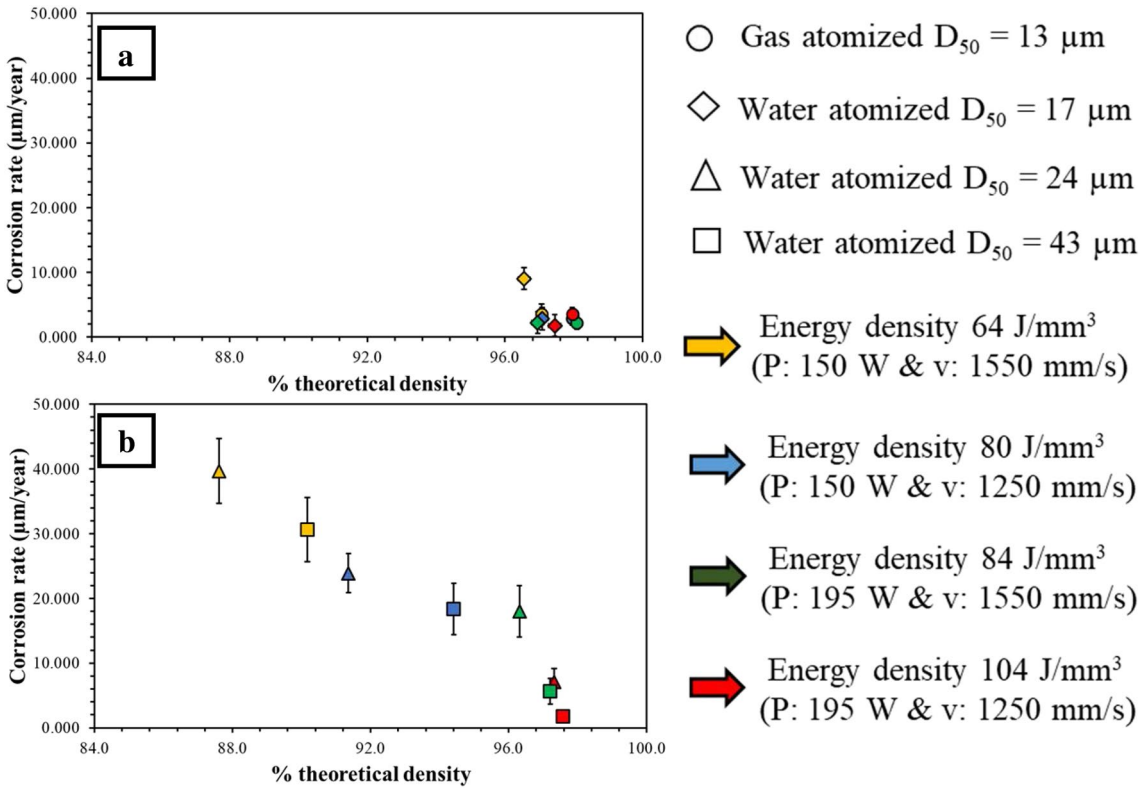

Fig. 8 Variation in corrosion rate as a function of % theoretical density and energy density for samples fabricated using: **a** gas-atomized (D_{50} = 13 µm) and water-atomized (D_{50} = 17 µm) powders; **b** water-atomized (D_{50} = 24 and 43 µm) powders. The symbols represent the four powders and the colors represent the four energy densities used in the fabrication

steel L-PBF parts is strongly dependent on their density, which in turn depends on the powder characteristics and L-PBF processing conditions.

Figure 8 shows the variation in corrosion rate as a function of the L-PBF parts density when fabricated at various energy densities using the four 17-4 PH stainless steel powders. The L-PBF parts fabricated using the finer gas (D_{50} = 13 µm) and water-atomized (D_{50} = 17 µm) powders ranged between 1 and 8 µm/year at different energy densities as shown in Fig. 8a. For further comparison, the corrosion rates of finer gas (D_{50} = 13 µm) and water-atomized (D_{50} = 17 µm) L-PBF parts were lower than that of the wrought 17-4 PH stainless steel is 3 ± 0.5 µm/year except at an energy density 64 J/mm^3. However, the corrosion rate for samples fabricated using the coarser water-atomized (D_{50} = 24 and 43 µm) powders decreased with an increase in energy density (Fig. 8b). At energy densities of 64 and 80 J/mm^3, the corrosion rate of the coarser water-atomized (D_{50} = 24 and 43 µm) L-PBF parts varied between 20 and 45 µm/year. These corrosion rate values are higher than that of the finer gas (D_{50} = 13 µm) and water-atomized (D_{50} = 17 µm) L-PBF parts fabricated at the same energy densities as well as the wrought samples. However, at an energy density of 104 J/mm^3, the corrosion rates were similar for L-PBF parts fabricated using all four powders (Fig. 8).

Figure 9 shows the optical microscopy images of the surfaces of samples fabricated at 64 J/mm^3 obtained before and after conducting potentiostatic polarization experiments. A significant difference was observed in the images before and after the corrosion tests for the coarser water-atomized (D_{50} = 24 and 43 µm) L-PBF parts at energy density 64 J/mm^3 as evidenced by an increase in a number of pores. In addition, relatively large pores were seen in the L-PBF parts fabricated using coarser water-atomized (D_{50} = 24 and 43 µm), whereas relatively smaller pores were found in L-PBF parts fabricated using finer gas (D_{50} = 13 µm) and water-atomized (D_{50} = 17 µm) powders before and after the potentiostatic polarization experiments. The presence of minor pores in the finer gas (D_{50} = 13 µm) and water-atomized (D_{50} = 17 µm) L-PBF parts after the corrosion tests could indicate the high resistance of the L-PBF parts to the corrosion phenomena [20, 22, 33, 36, 37]. The pore formation in the L-PBF parts after the corrosion tests is consistent with the quantitative data (Figs. 6, 7, 8) that the corrosion performance of L-PBF parts fabricated using finer gas (D_{50} = 13 µm) and water-atomized (D_{50} = 17 µm) powders are superior to the L-PBF parts fabricated using

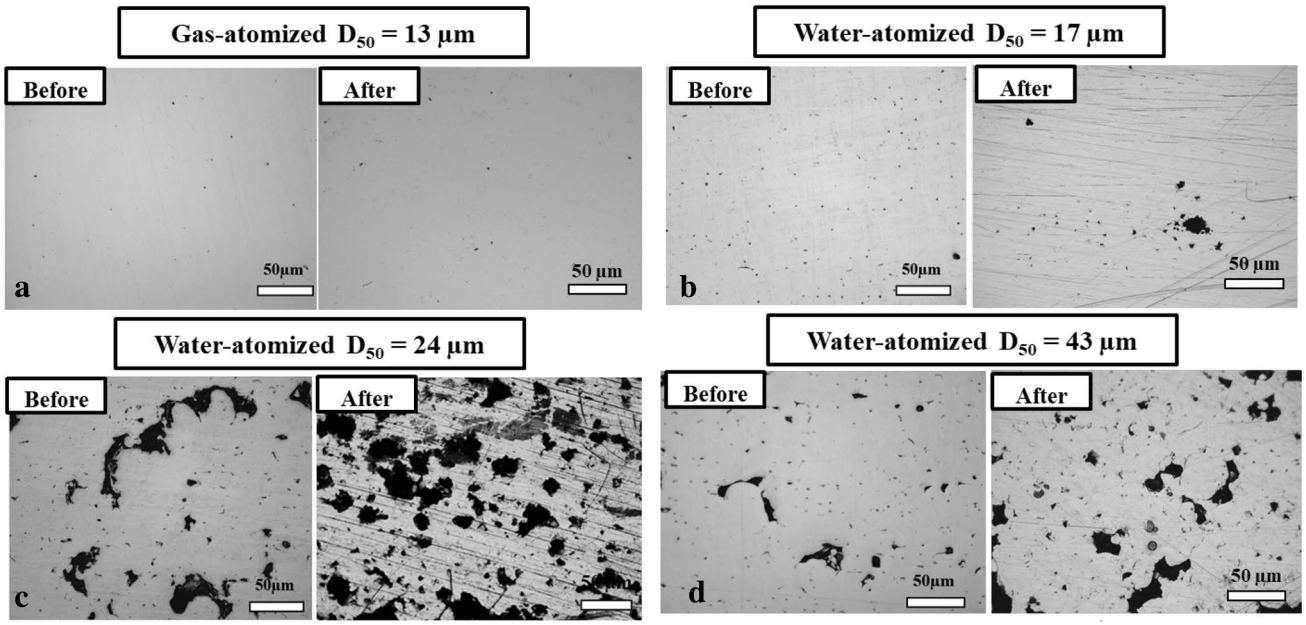

Fig. 9 Optical microscopy of samples fabricated at energy density 64 J/mm^3 using four 17-4 PH stainless steel powders acquired before and after conducting potentiostatic polarization experiments in 0.5 M NaCl solution

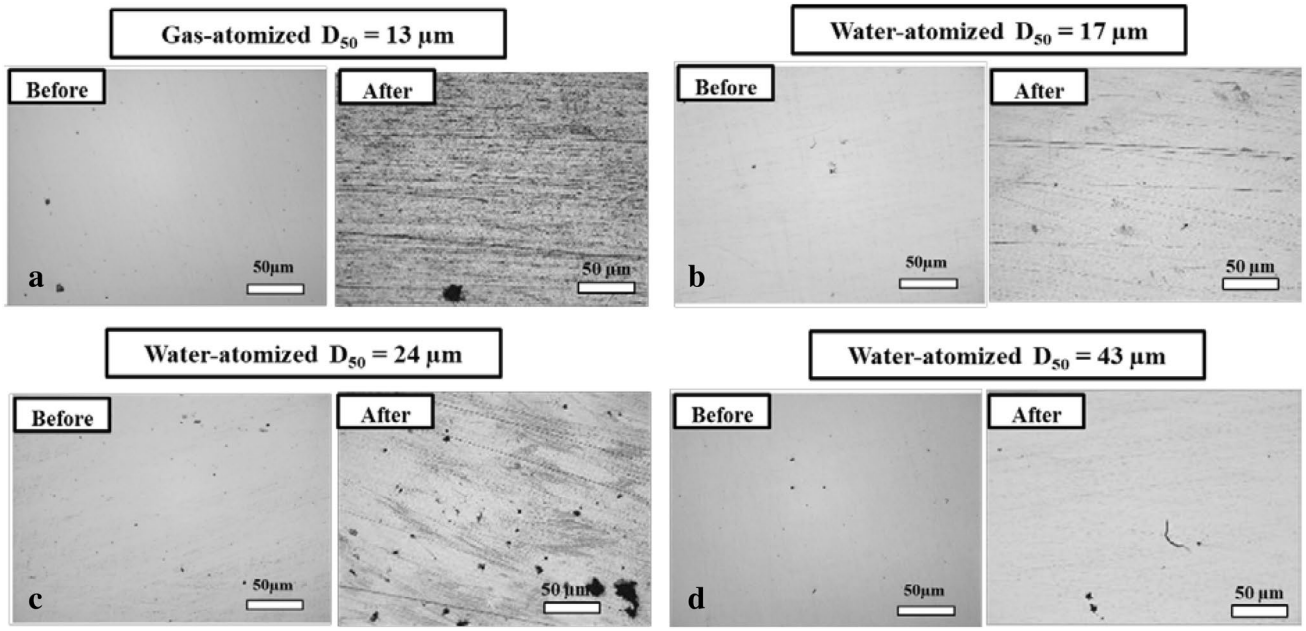

Fig. 10 Optical microscopy of samples fabricated at energy density 64 J/mm^3 using four 17-4 PH stainless steel powders acquired before and after conducting potentiostatic polarization experiments in 0.5 M NaCl solution

water-atomized powders (D_{50} = 17 and 43 µm) at an energy density of 64 J/mm^3.

Figure 10 shows the optical microscopy images of the surfaces of samples fabricated at 104 J/mm^3 obtained before and after conducting potentiostatic polarization experiments. Compared to the images presented in Fig. 9, low porosity parts were produced in all conditions. In addition, relatively fewer and finer pitting-induced pores were found after corrosion tests for all L-PBF parts. Further, the qualitative trends in optical images seen in all L-PBF parts at energy density 104 J/mm^3 are consistent with the corrosion performance data extracted from the Tafel plots (Figs. 6, 7, 8).

The porosity formed during the L-PBF process play a critical role in the initiation of pitting corrosion in the L-PBF parts. The pore geometry at low densities appears to be favorable for pitting corrosion since the pores would lead to stagnation of the sodium chloride solution in part [20, 22, 33, 36, 37]. The stagnation of chloride solution could cause a breakdown of the passive layer ensuing favorable sites for initiation of pitting corrosion and increases the rate of corrosion [20, 22, 33, 36, 37]. The L-PBF parts with densities higher than 97%, available pore sites desirable for pitting corrosion were less and could have decreased the rate of corrosion in the L-PBF parts [20, 38–40]. The rate of electrochemical corrosion reaction can be expressed as corrosion current in the L-PBF parts and decreases for the dense parts of the thick oxide layer. The decrease in the rate of electrochemical corrosion reactions could decrease the corrosion current of the L-PBF parts densities higher than 97% [20, 38–40].

Future experiments on densification and corrosion performance of 17-4 PH stainless steel L-PBF parts are currently being performed using hot isostatic pressing (HIP). Additionally, impedance tests will be performed to compare the corrosion performance of the L-PBF parts with the experimental data reported in this study. Further, surface analysis and impedance tests will be performed on the gas- and water-atomized L-PBF parts to understand the mechanisms of pit formation and corrosion performance as a function of microstructure and the results will be reported elsewhere.

4 Conclusions

The following conclusions were drawn from this study to understand the effects of processing conditions (energy density) and powder characteristics (shape and size) on the corrosion performance of 17-4 PH stainless steel parts produced by laser-powder bed fusion (L-PBF):

1. The corrosion performance of the 17-4 PH stainless steel L-PBF parts fabricated using gas- and water-atomized powders strongly depend on their density. The density and consequently the corrosion current, polarization resistance, corrosion rate of the L-PBF parts did not significantly vary for high dense ($97 \pm 0.5\%$) finer gas ($D_{50} = 13$ µm) and water-atomized ($D_{50} = 17$ µm) powders when fabricated using energy densities in the range from 64 to 104 J/mm^3. Furthermore, the corrosion performance of L-PBF parts of high density ($97 \pm 0.5\%$) showed slightly higher corrosion performance compared to the wrought sample.
2. The density and consequently the corrosion performance of coarser water-atomized powders ($D_{50} = 24$ and 43 µm) of L-PBF parts increased with energy density when fabricated in the same range of energy densities 64–104 J/mm^3.
3. At energy densities of 64, 80, 84 J/mm^3, L-PBF parts fabricated using the finer gas-atomized ($D_{50} = 13$ µm) and water-atomized ($D_{50} = 17$ µm) powders showed significantly better corrosion performance compared to coarser water-atomized powders ($D_{50} = 24$ and 43 µm) L-PBF parts.
4. At the energy density of 104 J/mm^3, the corrosion performance is independent of starting powder characteristics (shape and size) and atomization method (gas or water-atomization) used to produce these powders.
5. At the energy densities of 104 J/mm^3, the L-PBF parts fabricated using water-atomized powders ($D_{50} = 17$ and 43 µm) powders exhibited higher polarization resistance ($28{,}000 \pm 500$ Ω) than wrought samples ($25{,}000 \pm 1000$ Ω) in the 0.5 M NaCl environment.

Acknowledgements The authors thank the Walmart Foundation for funding the research project.

References

1. Irrinki H, Dexter M, Barmore B, Enneti R, Pasebani S, Badwe S, Stitzel J, Malhotra R, Atre SV (2016) Effects of powder attributes and laser powder bed fusion (L-PBF) process conditions on the densification and mechanical properties of 17-4 PH stainless steel. JOM 68:860–868
2. Gu H, Gong H, Pal D, Rafi K, Starr T, Stucker B (2013) Influences of energy density on porosity and microstructure of selective laser melted 17-4PH stainless steel. In: 2013 Solid Freeform Fabrication Symposium, p 474
3. Murr LE, Martinez E, Hernandez J, Collins S, Amato KN, Gaytan SM, Shindo PW (2012) Microstructures and properties of 17-4 PH stainless steel fabricated by selective laser melting. J Mater Res Technol 1:167–177
4. Lebrun T, Tanigaki K, Horikawa K, Kobayashi H (2014) Strain rate sensitivity and mechanical anisotropy of selective laser melted 17-4 PH stainless steel. Mech Eng J 1:SMM0049
5. Abe F, Osakada K, Shiomi M, Uematsu K, Matsumoto M (2001) The manufacturing of hard tools from metallic powders by selective laser melting. J Mater Process Technol 111:210–213
6. Murr LE, Martinez E, Amato KN, Gaytan SM, Hernandez J, Ramirez DA, Shindo PW, Medina F, Wicker RB (2012) Fabrication of et al and alloy components by additive manufacturing: examples of 3D materials science. J Mater Res Technol 1:42–54
7. Averyanova M, Bertrand P, Verquin B (2010) Effect of initial powder properties on final microstructure and mechanical properties of parts manufactured by selective laser melting. In: Annals of DAAAM for 2010 and Proceedings of the 21st International DAAAM Symposium, Vol 21
8. Spierings AB, Levy G, Wegener K (2012) Designing material properties locally with additive manufacturing technology SLM. In: Solid Freeform Fabrication Symposium
9. Song B, Dong S, Coddet P, Liao H, Coddet C (2014) Fabrication of NiCr alloy parts by selective laser melting: Columnar microstructure and anisotropic mechanical behavior. Mater Des 53:1–7

10. Facchini L, Vicente N, Lonardelli I, Magalini E, Robotti P, Molinari A (2010) Metastable austenite in 17-4 precipitation-hardening stainless steel produced by selective laser melting. Adv Eng Mater 12:184–188
11. Simchi A, Asgharzadeh H (2004) Densification and microstructural evaluation during laser sintering of M2 high speed steel powder. Mater Sci Technol 20:1462–1468
12. Simchi A (2006) Direct laser sintering of metal powders: mechanism, kinetics and microstructural features. Mater Sci Eng A 428(1–2):148–158
13. Pinkerton AJ, Li L (2005) Direct additive laser manufacturing using gas- and water-atomised H13 tool steel powders. Int J Adv Manuf Technol 25:471–479
14. Simchi A, Petzoldt F, Pohl H (2001) Direct metal laser sintering: Material considerations and mechanisms of particle bonding. Int J Powder Metall Princet N J 37:49–61
15. Fedrizzi A, Pellizzari M, Zadra M (2012) Influence of particle size ratio on densification behaviour of AISI H13/AISI M3:2 powder mixture. Powder Technol 228:435–442
16. Stoudt M, Ricker R, Lass E, Levine LE (2017) Influence of post-build microstructure on the electrochemical behavior of additively manufactured 17-4 PH stainless steel. JOM 69:506–515
17. Zeng L, Xiang N, Wei B (2014) A comparison of corrosion resistance of cobalt-chromium-molybdenum metal ceramic alloy fabricated with selective laser melting and traditional processing. J Prosthet Dent 112:1217–1224
18. Kurian A, Siva PM (2015) A comparison of corrosion resistance of stainless steel fabricated with selective laser melting and conventional processing. Int J Chem Tech Res 7:2632–2635
19. Zhao B, Wang H, Qiao N, Wang C, Hu M (2010) Corrosion resistance characteristics of a Ti-6Al-4V alloy scaffold that is fabricated by electron beam melting and selective laser melting for implantation in vivo. Mater Sci Eng C Mater Biol Appl 70:32–41
20. Costa I, Rogero SO, Saiki M, Marques RA, Rogero J,R (2008) Corrosion resistance and cytotoxicity study of 17-4PH steels produced by conventional metallurgy and powder injection molding. Mater Sci Forum 591:18–23
21. Singh AK, Reddy GM, Rao KS (2015) Pitting corrosion resistance and bond strength of stainless steel overlay by friction surfacing on high strength low alloy steel. Def Technol 11:299–307
22. Mudali UK, Bhaduri AK, Gnanamoorthy JB (1999) Localised corrosion behaviour of 17-4 PH stainless steel. Mater Sci Technol 6:475–481
23. Dos Santos AG, Biehl LV, Antonini LM (2017) Effect of chemical passivation treatment on pitting corrosion resistance of AISI 410 and 17–4 PH stainless steels. Mater Corros 68:824–830
24. Pulikkottil VJ, Chidambaram S, Bejoy PU, Femin PK, Paul P, Rishad M (2016) Corrosion resistance of stainless steel, nickel-titanium, titanium molybdenum alloy, and ion-implanted titanium molybdenum alloy archwires in acidic fluoride-containing artificial saliva: an in vitro study. J Pharm Bioallied Sci 8:6–9
25. Costa I, Franco CV, Kunioshi CT, Rossi JL (2006) Corrosion resistance of injection-molded 17-4PH steel in sodium chloride solution. Corrosion 62:57–65
26. Yanjin L, Yiliang G, Junjie L, Sai G, Songquan W, Jinxin L (2016) Effect of laser speeds on the mechanical property and corrosion resistance of CoCrW alloy fabricated by SLM. Rapid Prototyp J 16:28–33
27. Szewczyk-Nykiel A, Kazior J (2017) Effect of aging temperature on corrosion behavior of sintered 17-4 PH stainless steel in dilute sulfuric acid solution. J Mater Eng Perform 26:3450–3456
28. Irrinki H, Samuel J, Pasebani S, Badwe S, Stitzel J, Kate K et al (2018) Effects of particle characteristics on the microstructure and mechanical properties of 17-4 PH stainless steel fabricated by laser-powder bed fusion. Powder Technol 331:192–203
29. Lee YS, Zhang W (2015) Mesoscopic simulation of heat transfer and fluid flow in laser powder bed additive manufacturing. In: Proceedings of the Annual International Solid Freeform Fabrication Symposium, pp 10–12
30. Olakanmi EO (2012) Effect of mixing time on the bed density, and microstructure of selective laser sintered (sls) aluminium powders. Mater Res 15:167–176
31. Liu B, Wildman R, Tuck C, Ashcroft I, Hague R (2011) Investigation the effect of particle size distribution on processing parameters optimisation in selective laser melting process. Addit Manuf Res Group 227–238
32. Manakari V, Parande G, Gupta M (2016) Selective laser melting of magnesium and magnesium alloy powders: a review. Metals 7(2):1–35
33. Frankel GS (2016) Fundamentals of corrosion kinetics. Active Prot Coat 17–32.
34. Geenen K, Röttger A, Theisen W (2017) Corrosion behavior of 316L austenitic steel processed by selective laser melting, hot-isostatic pressing, and casting. Mater Corros 68:764–775
35. Schaller RF, Taylor JM, Rodelas J, Schindelholz EJ (2015) Corrosion properties of powder bed fusion additively manufactured 17-4 PH stainless steel. Corrosion 73:796–807
36. Klar E, Samal PK (2007) Powder metallurgy stainless steels: processing, microstructures, and properties. In: ASM international, vol 1, pp 77–95
37. Samal PK, Hu B, Hauer I, Mars O (2008) Optimization of corrosion resistance and machinability of PM 316L stainless steel. In: Advances in powder metallurgy and particulate materials, pp 740–750
38. Raja KS, Rao KP (1995) Pitting behavior of type 17-4 PH stainless steel weldments. Corrosion 51:586–592
39. Lai C, Xiang Z (2015) Investigation the effect of porosity on corrosion of macroporous silicon in 1.0 M sodium hydroxide solution using weight loss measurements, electrochemical methods and scanning electron microscope. Corros Sci 99:178–184
40. Aghion E, Perez Y (1995) Effects of porosity on corrosion resistance of Mg alloy foam produced by powder metallurgy technology. Mater Charact 96:78–83